



DRIFTS-SSITKA-MS investigations on the mechanism of plasmon preferentially enhanced CO₂ hydrogenation over Au/γ-Al₂O₃

Ke Wang ^{a,b,1}, Shibo Shao ^{b,e,1}, Yanrong Liu ^a, Mengyu Cao ^{b,d}, Jialin Yu ^b, Cher Hon Lau ^b, Ying Zheng ^c, Xianfeng Fan ^{b,*}

^a Beijing Key Laboratory of Ionic Liquids Clean Process, CAS Key Laboratory of Green Process and Engineering, State Key Laboratory of Multiphase Complex Systems, Innovation Academy for Green Manufacture, Institute of Process Engineering, Chinese Academy of Sciences, Beijing 100190, China

^b Institute for Materials and Processes, School of Engineering, the University of Edinburgh, Edinburgh EH9 3FB, Scotland, UK

^c Department of Chemical and Biochemical Engineering, Western University, London, Ontario, N6A 5B9 Canada

^d SINOPEC (Beijing) Research Institute of Chemical Industry Co., Ltd, Beijing 100013, PR China.

^e Petrochemical Research Institute, PetroChina Company Limited, Beijing 102206, China



ARTICLE INFO

Keywords:

Localized surface plasmon resonance (LSPR)

Reverse water gas shift (RWGS) reaction

In-situ DRIFTS-MS

Photo-thermo coupling mechanism

CO₂ reduction

ABSTRACT

The localized plasmon resonance (LSPR) is recognized as an effective way to convert incident light energy and significantly boost the catalytic reaction. However, a comprehensive understanding of the plasmon-thermo coupling mechanism is still lacking. To address this knowledge gap, we investigate reaction pathway and plasmonic enhancement mechanism of the photo-thermo coupled catalytic reverse water gas shift (RWGS) reactions over Au/γ-Al₂O₃. The results indicate that both formate and carboxyl pathways contribute to the overall reaction. The m-formate pathway is suggested as the main reaction mechanism at low reaction temperature over small Au NPs. Spectro-kinetics and theoretical calculation analyses indicate that the plasmonic energy preferentially transfers to HCOO^{*} via a combination of hot electron and resonance energy transfer mechanisms. The plasmonic energy facilitates the dehydration of HCOO^{*} to CO, which is the rate-determining step (RDS) of the overall RWGS reaction.

1. Introduction

As the abrupt rise of CO₂ levels in the atmosphere shows more evidence of its effects on climate change, effective catalytic CO₂ conversion becomes essentially important to achieve carbon neutrality [1]. To fulfil this target, the conversion of CO₂ is ideally driven by renewable energy. Catalytic metallic nanoparticles (NPs) harvest light energy and transfer to CO₂ reduction reaction via the localized surface plasmonic resonance (LSPR) excitation and damping has been proven to be a promising way to couple photo- and thermo-catalysis [2,3]. In recent literature, most of the works reported their contributions to the catalysts design to boost the photo-thermo catalytic CO₂ reduction rate [4–6]. In addition to the enhanced CO₂ reduction rate, the incident light was also reported to alter the product selectivity of CO₂ reduction [7,8], which makes the coupling of light irradiation with thermocatalysis a promising way to selectively synthesize high-value products. However, the lacking of unequivocal understanding of the mechanism underpinning the

photo-thermo coupling hinders the rational design of both the catalysts and the entire process [9].

Reverse water gas shift (RWGS) is a great model reaction to investigate the photo-thermo coupling mechanism, because there are two generally believed associative mechanisms (formate and carboxyl pathways) leading to one simple product of CO. More importantly, RWGS is usually the first and most critical step for the synthesis of other value-added products including methanol, methane and higher alcohol or hydrocarbons [10], whereas the RWGS mechanism is still an unresolved question and largely dependent on the catalyst supports investigated. In the specific case of using Al₂O₃ as catalyst supports, the role of formate in RWGS reaction is still under debate. For example, Szanyi et al. [11,12] proposed that CO₂ hydrogenation to CO followed the carboxyl pathway on the Pd/Al₂O₃ rather than the formate pathway. A metastable under-coordinated Pd active sites were formed during the reaction. Conversely, Bobadilla et al. [13] suggested that the fast formate route was the main reaction pathway and most of the formate

* Corresponding author.

E-mail address: x.fan@ed.ac.uk (X. Fan).

¹ These authors contribute equally to this work.

on the surface still remained as spectators. The bicarbonate group acted as the intermediate for the formation of formate. Similarly, Wang et al. [14] claimed the similar bicarbonate-formate mechanism for CO₂ hydrogenation on Ru/Al₂O₃ and Pd/Al₂O₃. In summary, the actual reaction mechanism of RWGS over Al₂O₃ supported catalysts is still an unresolved challenge.

In-situ characterizations are the ideal techniques to unravel the reaction and photo-thermo coupling mechanisms [15]. Isotope-labelled spectrokinetics analyses of chemical species on the surface are one of the most accurate ways to identify the reaction pathway [16,17]. For example, Wang et al. [18] used steady-state isotope transient kinetic analysis-mass spectroscopy (SSITKA-MS) technique to investigate the photo-thermo coupling mechanism of RWGS reaction over Au/TiO₂. The spectrokinetic analyses clearly ruled out the formate pathway and supported the redox pathway in both dark and light irradiation conditions. The photo-thermo coupling mechanism was proven to be the plasmon-excited “hot” electrons facilitating the generation of oxygen vacancies (V_O). Deng et al. [19] suggested that the plasmonic enhancement of RWGS over Cu-Ga/CeO₂ corresponded to the “hot” electrons-facilitated H₂ dissociation and formate decomposition. Additionally, the involvement of reducible catalyst supports usually enlarges the influences of plasmonic “hot” electrons due to the enhanced charge separation [20,21]. Only a few works ascribed the plasmonic enhancement to other energy transfer mechanism. For instance, Xu et al. [22] attributed the enhanced CO₂ reduction to the plasmon induced local electromagnetic field. To date, whether or how other plasmonic enhancement mechanisms including direct/indirect mechanisms and resonance energy transfer contribute to the photo-thermo catalytic process is still largely unknown.

In this work, we investigate photo-thermo coupled catalytic RWGS reaction over Au/γ-Al₂O₃ with similar Au loading but Au NPs in different sizes to elucidate both the RWGS reaction pathways as well as the plasmonic enhancement mechanism. The usage of nonreducible and wide-bandgap γ-Al₂O₃ provides a well-defined model for impartial evaluation to the different plasmonic promotion effects towards thermocatalytic RWGS reaction. Different Au NPs sizes, which fundamentally determine the LSPR strength, help to explicitly elucidate the mechanisms underpinning plasmonic enhancement on reaction kinetics. The catalytic activity under photo-thermo coupled condition is increased by a maximum of 211.8 % comparing with a pure thermocatalytic reaction. The non-thermal effects of LSPR are confirmed by the enlarged H/D kinetic isotope effects (KIE). The reaction mechanisms both in thermal and photo-thermo coupled conditions are analysed by a series of isotope-labelled *in-situ* DRIFTS-MS experiments. It is found that both carboxyl and formate pathways contribute to the production of CO, while the proportions of their contributions vary with Au size and irradiation conditions. For Au/Al₂O₃ with small Au NP size, the monodentate formate (m-HCOO^{*}) is suggested as the main reaction pathway. Moreover, the plasmonic resonance preferentially enhances the kinetics of HCOO^{*} intermediates, which in turn facilitates the overall reaction rate. Electronic structure analyses suggest that the plasmonic energy transfer mechanism includes both “hot” electron injection and resonance energy transfer mechanism, which are also Au NPs size-dependent.

2. Experimental

2.1. Materials

Isotopic gases including ¹³CO₂ (99 % atom ¹³C) Deuterium gas (D₂, 99 % atom D) are purchased from Sigma-Aldrich. High purity gases in zero, research or CP grade including Air, Ar, H₂ and CO₂ are supplied by BOC limited, UK. Commercial γ-Al₂O₃ supplied by Alfa-Aesar is used as support of catalysts. HAuCl₄·3 H₂O and urea are purchased from ACROS organics.

2.2. Catalysts preparation

Au/γ-Al₂O₃ was prepared following the conventional deposition-precipitation (DP) method. 2 mmol HAuCl₄·3 H₂O and 200 mmol urea were dissolved in 100 mL water and agitated with a magnetic stirrer bar. The beaker with the solution was wrapped with aluminum foil to rule out the interference from ambient light. The solution was heated to 80 °C and held for 5 h in an oil bath. The catalysts were separated from the solution using a vacuum filtration method. Ultrapure water was used to rinse the catalyst 8 times to remove residual Cl⁻ ions. The powder was dried in a vacuum oven at 60 °C overnight. Calcination at 400, 600, 800 °C for 2 h was conducted for the dried powder in a muffle furnace. The ramping rate was set to be 1 °C min⁻¹. The samples calcined at 400, 600, 800 °C are denoted as Au/Al₂O₃-400, Au/Al₂O₃-600 and Au/Al₂O₃-800, respectively.

2.3. Physical characterizations

The loadings of Au in the catalysts were determined by inductively coupled plasma-optical emission spectroscopy (ICP-OES) method. 5 mg Au/Al₂O₃ was digested in 10 mL freshly prepared Aqua Regia at 120 °C for 12 h. The solution was further diluted to 100 mL with ultrapure water in a volumetric flask. The analytes were automatically analysed by the spectrometer (Varian Vista-Pro) equipped with an autosampler. The crystalline phase of the catalyst was characterized with an X-ray diffractometer (XRD, Bruker D2 Phaser). X-ray photoelectron spectroscopy (XPS) analyses were conducted with a Kratos Axis Ultra DLD spectrometer. XPS spectra were calibrated to adventitious C1s of 284.6 eV [18]. The detailed morphologies of the catalysts and Au NP sizes were characterized with high-angle angular dark-field scanning transmission electron microscopy method (HAADF-STEM, FEI Titan Themis 200). The specific surface areas of catalysts were measured with N₂ sorption method at 77 K (Quantachrome Autosorb iQ). The ultraviolet-visible light absorption was characterized in diffuse reflectance spectroscopy method (UV-Vis DRS) with an UV-Vis spectrometer (Shimadzu UV-3600 plus) equipped with a praying mantis accessory. The spectrum of BaSO₄ powder was used as the background at room temperature. CO₂-temperature programmed desorption (CO₂-TPD) experiment was conducted with automatic sorption analyser (Autosorb-iQ, Quantachrome) equipped with a MS (Hidden, RGA201). 50 mg Au/Al₂O₃ was packed into a quartz U-shape reactor and pretreated at 800 °C in flowing He (50 sccm) for 30 min to achieve a clean surface. Then CO₂ flowed into the reactor for 30 min at 30 °C to achieve an equilibrium. Then the cell was purged with He flow (50 sccm) for 1 h and ramp to 800 °C at a rate of 10 °C min⁻¹. The installed MS was used to monitor the evolution of CO₂ concentration with *m/z* = 44.

2.4. CO₂ hydrogenation performance evaluation

CO₂ hydrogenation performance evaluation was conducted with a commercial DRIFTS *in-situ* reactor, as shown in Fig. S1. The temperature was calibrated with a thermocouple inserted into the powder from the bottom. 1 sccm CO₂ and 4 sccm H₂ balanced with Ar into 30 sccm in total were controlled by mass flow controllers and introduced into the reactor. The inlet and outlet gas lines temperatures were controlled by a PID temperature controller and kept at 130 °C to prevent any condensation. The effluent gas from the vent of the reactor was analysed by a gas chromatograph (Shimadzu GC-2010 plus) equipped with a thermal conductivity detector (TCD) and a flame ionization detector (FID). A micro-packed carbon molecular sieve column (Restek, ShinCarbon ST column) was used to separate the products from permanent gases. An external green LED was used as the external source to promote the reaction, which was introduced into the reactor via a liquid light guide. The power intensity of the green light was measured to be 250.1 mW cm⁻² with a thermopile optical power meter (Thorlabs, PM601).

The H/D kinetic isotope effect (KIE) and equilibrium isotope effect

(EIE) were measured using the same setup by replacing H₂ with D₂. The flow of D₂ was maintained the same to the H₂ flow rate by regularly checking with an electronic flow meter. The KIE value was equal to the ratio of the reaction rate (r_{CO}) with H₂ over the r_{CO} with D₂. The EIE value was determined by comparing the concentration of hydrogenated bicarbonate and deuterated bicarbonate. The details are described in the supporting information (SI-Section 4).

2.5. In-situ DRIFTS-MS analyses

All *in-situ* DRIFTS-MS experiments were conducted with the setup shown in Figs. S1&S2. To achieve a reliable identification of species via DRIFT spectra, control experiments with isotope gas were conducted over our own catalysts. The careful deconvolution and peak assignments results are presented in SI-Section 3.1 (Figs. S7&S8, Tables S1&S2).

2.5.1. Reaction mechanism investigation with temperature-programmed surface reaction (TPSR) via DRIFTS-MS

The reaction mechanisms in dark or under green light irradiation were investigated via TPSR. The evolved surface species and effluent gaseous products were *in-situ* monitored by DRIFTS-MS technique ($m/z = 18, 29, 45$ for H₂O vapor, ¹³CO and ¹³CO₂, respectively). 10 mg catalysts were packed into the reactor sample cup each time. The catalysts were *in-situ* treated at 400 °C under flowing Air and Ar in sequence for 30 min, respectively, to achieve a clean surface for spectroscopy analyses. After cooling down naturally to 30 °C, 1 sccm ¹³CO₂, 4 sccm H₂, 25 sccm Ar were controlled by mass flow controllers and premixed before introduced into the reactor. The temperature of the reactor ramped to 480 °C in a rate of 10 °C min⁻¹. Using ¹³CO₂ instead of ¹²CO₂ can significantly increase the lower detection limit of CO by MS, because the intervention from N₂ is fully ruled out. Note that unambiguous results cannot be achieved by using ¹²CO₂.

2.5.2. Br-HCOO* role investigation with TPSR via DRIFTS-MS

A similar TPSR protocol was used to investigate the role of Br-HCOO* during the reaction. The catalysts were pre-treated in flowing Air and Ar in sequence, which is identical to the procedure described in the previous section. To *in-situ* create br-HCOO* species on the surface of Au/ γ -Al₂O₃, the reactant gas mixture (1 sccm ¹³CO₂, 4 sccm H₂, 25 sccm Ar) was introduced into the reactor at 300 °C for 20 min. This step is identical to the catalytic performance evaluation. Then the inlet gas mixture was swiftly switched to either H₂/Ar mixture (4 sccm/25 sccm) or pure Ar (30 sccm in the buffering line). Simultaneously, the reactor was cooled down to room 30 °C naturally. Since the temperature of the reactor side wall is controlled by water circulation with a chiller working at 25 °C, the cooling down process will always take ~20 min. After stabilizing at 30 °C, the reactor was ramped to 480 °C with a rate of 10 °C min⁻¹. The evolution of H¹³COO* on surface and effluent gases were monitored by DRIFTS and MS ($m/z = 18, 29, 45$ for H₂O vapor, ¹³CO and ¹³CO₂, respectively). The TPSR experiments were conducted under dark and green light irradiation, respectively, to elucidate the plasmonic enhancement mechanism.

2.5.3. SSITKA-DRIFTS experiments

The catalysts were pretreated in Air and Ar at 400 °C for 30 min in sequence to achieve a clean surface. After cooling down to 300 °C, under Ar flowing, the BKG was collected. 1 sccm ¹²CO₂, 4 sccm H₂ balanced by Ar to 30 sccm in total was switchable with 1 sccm ¹²CO₂, 4 sccm H₂ and 0.5 sccm He balanced to 30 sccm by Ar. ¹²CO₂/H₂ was introduced into the reactor for at least 30 min at 300 °C until reaching steady state. ¹³CO₂/H₂ was switched via a 4-way switching valve. DRIFT spectra were recorded with a FTIR (Shimadzu IRTtracer-100) with a scanning rate of 3 spectra per minute.

2.6. Theoretical calculations

Spin-polarized density functional theory (DFT) calculations were conducted using the Quantum Espresso package [23] with Perdew-Burke-Ernzerhof (PBE) functional [24] at generalized gradient approximation (GGA) level. Semi-empirical Grimme-D3 dispersion correction [25] was applied to achieve a better description of long-range dispersion interaction. The nuclei and core electrons were described by ultrasoft pseudopotentials from GBRV library [26]. The wavefunctions and charge density were expanded with kinetic cutoff of 45 and 450 Ry, respectively. The first Brillouin zones of bulk γ -Al₂O₃ and slab model of Au₁₃/ γ -Al₂O₃ were sampled with Monkhorst-Pack k-points grids of 14 × 10 × 10 and 2 × 2 × 1, respectively. A gaussian smearing was added with 0.01 Ry width to accelerate the convergence. For optimization, the energy and force convergence criteria were set to be 5 × 10⁻⁵ Ry and 5 × 10⁻⁴ Ry Bohr⁻¹, respectively. The transition states were searched with the climbing image nudged elastic band (CI-NEB) [27] method with a convergence criterium of 0.05 eV Å⁻¹. Lobster code [28] was used to perform crystal orbital Hamilton population (COHP) analyses. The visualization of the calculation results was conducted with the VESTA [29] code. The CO₂ adsorption energy (E_{ad}) was calculated with following equation:

$$E_{ad} = E(CO_2^* + \text{slab}) - E(CO_{2,\text{gas}}) - E(\text{slab}) \quad (1)$$

3. Results and discussion

3.1. Catalyst characterizations

The Au loadings are determined via ICP-OES to be 3.62 ± 0.01 %, 3.58 ± 0.02 % and 3.75 ± 0.02 % for Au/Al₂O₃-400, Au/Al₂O₃-600 and Au/Al₂O₃-800, respectively. The Au/ γ -Al₂O₃ catalysts were characterized with XRD and the corresponding diffraction patterns are shown in Fig. S3(a). The diffraction peaks are in consistency with standard γ -Al₂O₃ pattern (JCPDS 029-0063) and small peaks corresponding to Au NPs (JCPDS 04-0784). The higher calcination temperature brings stronger diffraction peaks due to larger NP sizes. The specific surface area (SSA) of γ -Al₂O₃ and Au/ γ -Al₂O₃ are measured with N₂ sorption experiments (Fig. S3(b)). The derived Brunauer–Emmett–Teller (BET) SSAs are 111.5, 116.7 and 111.5 m² g⁻¹ for Au/Al₂O₃-400, Au/Al₂O₃-600, Au/Al₂O₃-800, respectively. Compared with the pristine γ -Al₂O₃ with SSA of 99.9 m² g⁻¹, the SSAs are not influenced by calcination temperature. From the above results, it can be concluded that the calculation temperature within the investigated range in this work shows less influence on the Au loadings and SSAs, which can be treated as insignificant factors in this work. Au NP size was characterized with HAADF-STEM images (Fig. 1). Based on measuring hundreds of NPs, the average diameters of Au NP dispersed on γ -Al₂O₃ are calculated to be 4.3, 6.7 and 31.3 nm corresponding to Au/Al₂O₃-400, Au/Al₂O₃-600, Au/Al₂O₃-800, respectively. The calcination temperature shows significant effects on the sizes of Au NPs. The different Au NP sizes and the different LSPR effects derived from the Au sizes are the main factors influencing the thermal and photo-thermo coupled reaction mechanisms. The XPS (Fig. S4) and UV-Vis DRS (Fig. S5) results in consistency with the Au size and the LSPR effect sequence are presented and discussed in the SI-Section 2.

3.2. Plasmonic enhancement of CO production

The CO₂ hydrogenation performances were evaluated at temperatures from 285 °C to 330 °C with a step of 15 °C. The performance results in dark or green light irradiation are shown in Fig. 2. In the case of reaction in dark, the Au size effects on CO production rate are significant. At 300 °C, the Au/Al₂O₃-400 with smallest Au NP size produces CO in a rate of 0.47 mmol g_{cat}⁻¹ h⁻¹, which is significantly higher than the counterparts of Au/Al₂O₃-600 (0.40 mmol g_{cat}⁻¹ h⁻¹) and Au/Al₂O₃-800

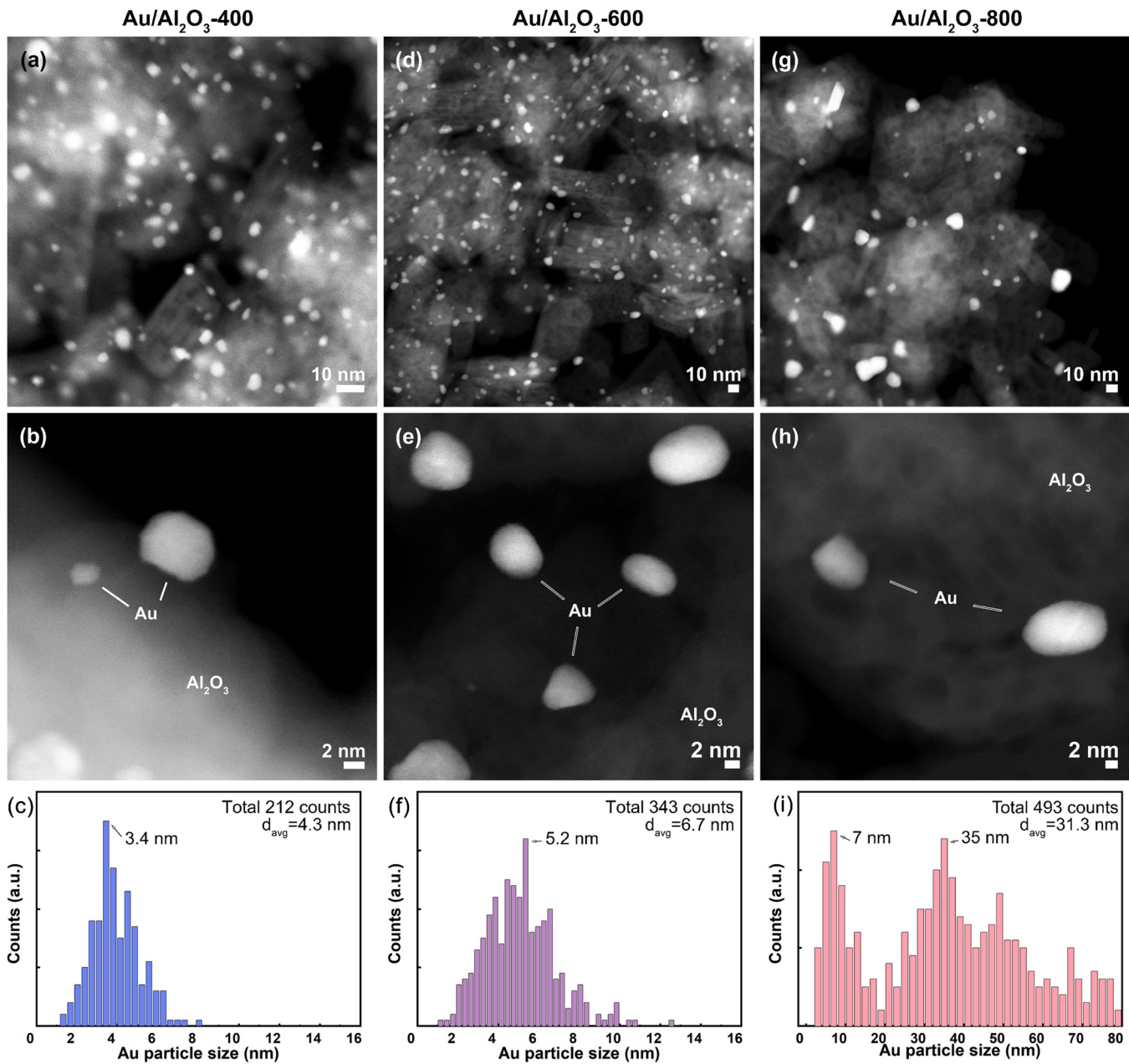


Fig. 1. HAADF-STEM images of (a, b) Au/Al₂O₃-400, (d, e) Au/Al₂O₃-600, (g, h) Au/Al₂O₃-800. (c, f, i) are the corresponding Au NP size distribution diagrams, respectively.

(0.17 mmol g_{cat}⁻¹ h⁻¹) with larger Au NPs. The inferior pure thermal catalytic performance of larger Au NPs is attributed to the much less Au/ γ -Al₂O₃ perimeter active sites for the reaction, especially for H₂ dissociation [18]. The corresponding activation energies in dark show the same sequence as presented in Fig. 2(d-f). Au/Al₂O₃-400 shows an activation energy of 50.6 kJ mol⁻¹ in dark, which is only 37.6 % of Au/Al₂O₃-800 (134.6 kJ mol⁻¹). By contrast, for reactions under green light irradiation, the plasmonic enhancement of CO production follows an inverted trend. At 300 °C under green light irradiation, the CO production rates are 211.8 %, 150.0 % and 142.5 % of the dark reaction rate for Au/Al₂O₃-400, Au/Al₂O₃-600 and Au/Al₂O₃-800, respectively. The more pronounced plasmonic enhancement is strongly related to the stronger LSPR effects, since the influences of loading and surface areas are similar across all 3 samples. The most significant plasmonic enhancement is also reflected by the reduction of activation energy compared with its counterpart in dark. The activation energy reduces by

2.1, 6.7 and 15.3 kJ mol⁻¹ for Au/Al₂O₃-400, Au/Al₂O₃-600 and Au/Al₂O₃-800 under green light irradiation, respectively. The Au NP sizes were further characterized via bright-field TEM images. As shown in Fig. S6, the Au NP sizes of spent catalysts did not show significant changes after 2-h reactions, which suggests the high stabilities of Au NPs under the photo-thermo coupled catalytic reaction conditions. In summary, the pronounced plasmonic enhancement differences across the 3 samples with different Au NP sizes, ensure them as great targets for thermo-photo coupling mechanism investigations.

3.3. Reaction mechanism and plasmonic enhancement mechanism over Au/Al₂O₃

Different from Au loaded on a reducible support [18,20], the redox mechanism of CO₂ over Au/Al₂O₃ is reasonably ruled out by control experiments in both dark and light-irradiated conditions (SI-Section

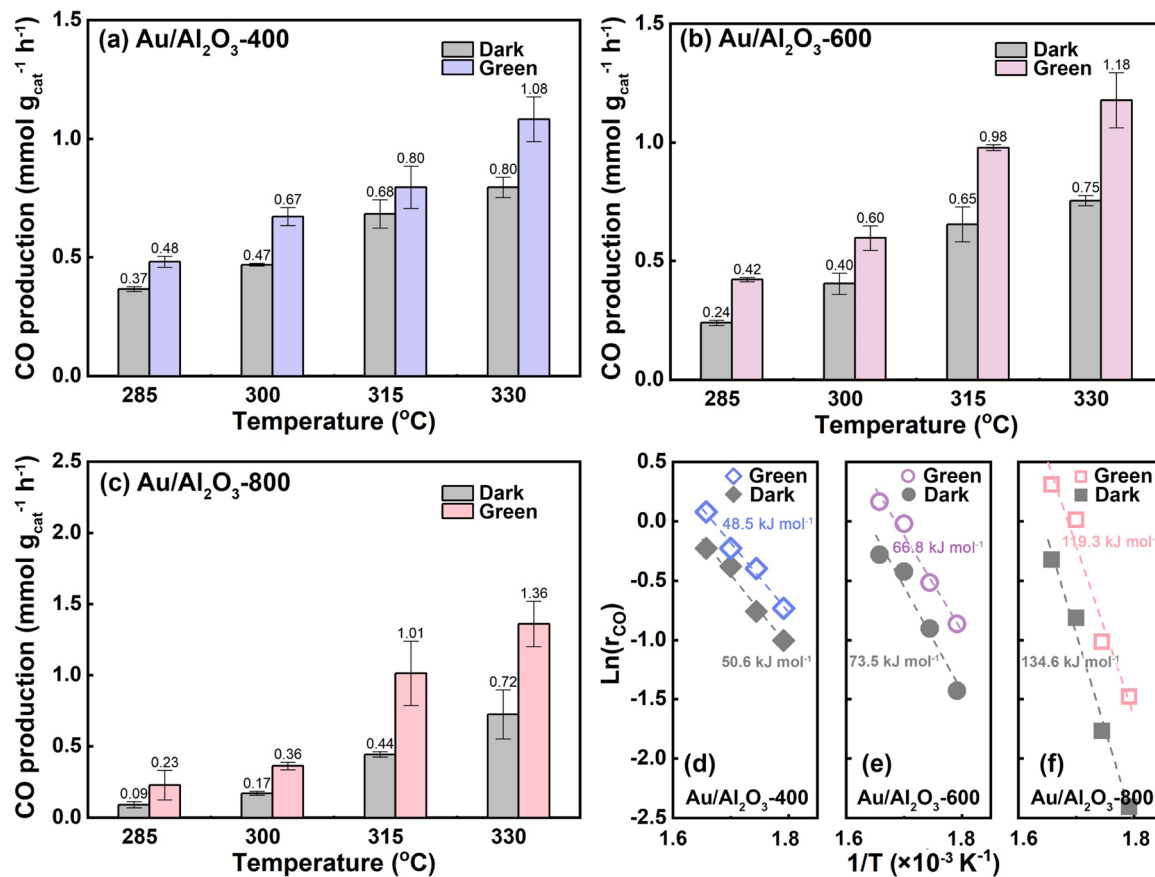


Fig. 2. CO production rates in dark and under green light irradiation over (a) Au/Al₂O₃-400, (b) Au/Al₂O₃-600 and (c) Au/Al₂O₃-800. The corresponding Arrhenius plots for (d) Au/Al₂O₃-400, (e) Au/Al₂O₃-600 and (f) Au/Al₂O₃-800.

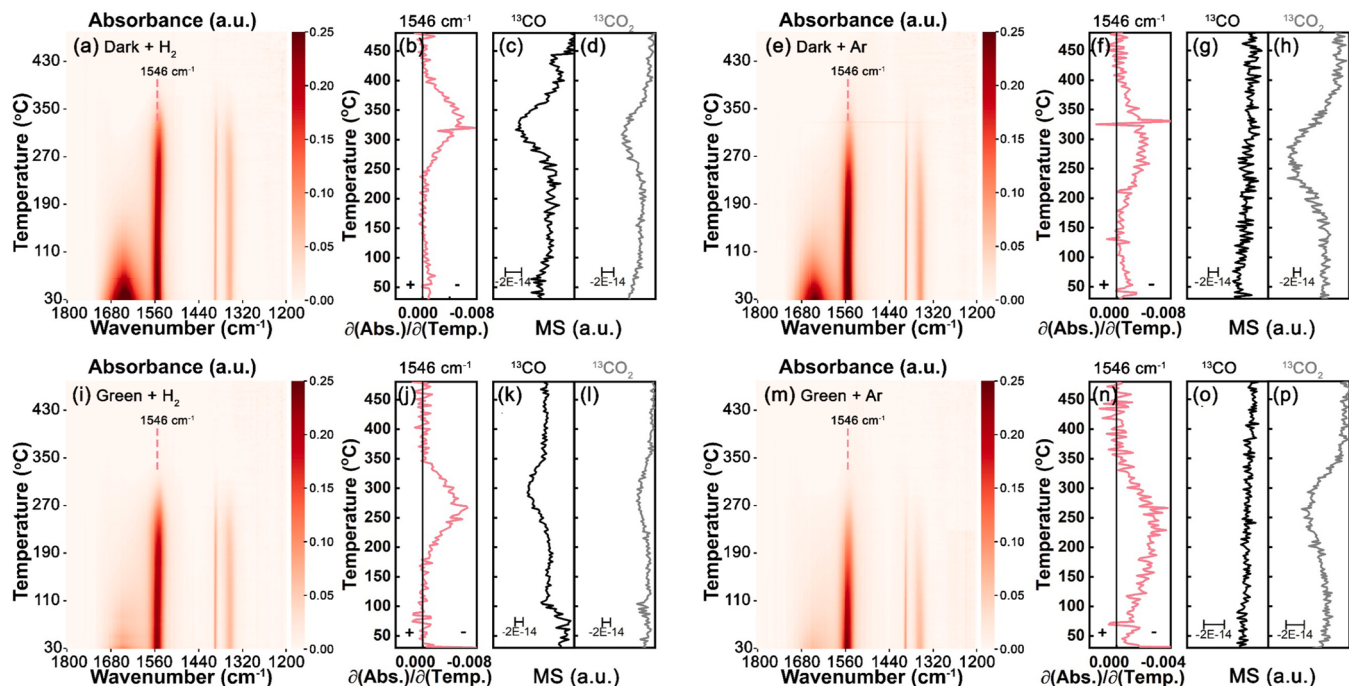


Fig. 3. Temperature-programmed surface reaction (TPSR) results achieved with DRIFTS-MS at different atmospheres and irradiation conditions over Au/Al₂O₃-400. Temperature-resolved DRIFT contours of br-HCOO* reduction in (a) dark + H₂, (e) dark + Ar, (i) green light + H₂, (m) green light + Ar. (b, f, j, n) The corresponding derivatives of br-HCOO* IR peak (1546 cm⁻¹) intensity with respect to temperature are plotted against temperature. The corresponding time-resolved MS signals of (c, g, k, o) ¹³CO and (d, h, l, p) ¹³CO₂, *m/z* = 29 and 45 are used for ¹³CO and ¹³CO₂ MS measurements, respectively.

3.2). As a result, the most plausible reaction pathways of RWGS over Au/Al₂O₃ are the carboxyl (COOH*) and formate (HCOO*) pathway [11]. Note that both the COOH* and HCOO* mainly exhibit bridged (br-) and monodentate (m-) configurations (Figs. S7&S8), their different contribution to the RWGS over Au/Al₂O₃ are not fully understood to date, especially under photo-thermo coupled reaction condition. In this section, a series of isotopic *in-situ* DRIFTS-MS experiments were used to elucidate the reaction mechanism in pure thermal and photo-thermo coupled reaction conditions.

3.3.1. Confirmation of br-formate as reaction intermediates

It has been a long debate on the role of formate during the CO₂ hydrogenation reaction [30–32], because formate is easy to form from CO₂* , while difficult to be further dehydrated due its high stability. Therefore, it is of great importance to prove that formate does contribute to the CO production in RWGS over Au/Al₂O₃, especially under photo-thermo coupled reaction condition. The key evidence to convince the formate pathway is to prove that the conversion of HCOO* will directly result in CO production.

To demonstrate the br-HCOO* hydrogenation to CO* mechanism in dark, the TPSR experiments were conducted under flowing H₂/Ar. The important control group of TPSR in flowing Ar w/o H₂ was also performed. The corresponding DRIFTS-MS results are shown in Fig. 3(a-d) and Fig. 3(e-h), respectively. In both conditions, the br-H¹³COO* can be clearly observed in DRIFT spectra contours (1546 cm⁻¹) after pretreatment with ¹³CO₂/H₂ at 300 °C for 20 min. Following with purging for more than 30 min can effectively remove the gaseous H₂ from the reactor. The symmetric peak of 1546 cm⁻¹ suggests that m-HCOO* is completely consumed during the purging step, which proves the high activity of m-HCOO*. To better illustrate the evolution of IR peak intensity of br-HCOO*, the derivative of absorbance with respect to temperature ($\partial\text{Abs.}/\partial\text{Temp.}$) is plotted against temperature. In the TPSR under flowing H₂/Ar (Fig. 3(a-d)), the consumption of br-HCOO* highly matches the effluence of ¹³CO, with the peak at the temperature of ~340 °C. On the contrary, with the absence of H₂ (Fig. 3(e-h)), the decomposition of br-HCOO* doesn't generate ¹³CO. The observed ¹³CO₂ is believed to be derived from the direct decomposition of H¹³COO* to ¹³CO₂* and H*. Moreover, there is no obvious formation of m-HCOO* during this experiment, which suggests the br-HCOO* might not have to first convert to m-HCOO*, then further produce CO. It is further supported by our DFT calculation result that br-HCOO* is more stable than m-HCOO* by 0.94 eV. From thermodynamics perspective, the equilibrium concentration ratio of br-HCOO* to m-HCOO* is rather low. Under an Ar atmosphere, the formation of m-HCOO* from br-HCOO* is still negligible too, which proves this transformation is also kinetically unfavorable. The similar comparison experiments were conducted under green light irradiation and the results are presented in Fig. 3(i-l) and Fig. 3(m-p). The same pronounced correlation between br-H¹³COO* consumption and ¹³CO production is also found in H₂/Ar atmosphere, while no ¹³CO is detected without H₂. In Fig. 3(j), the $\partial\text{Abs.}/\partial\text{Temp.}$ shows a center of ~280 °C, which is significantly lower than the corresponding temperature of ~330 °C in dark. The TPSR experiments under green light further confirms that br-HCOO* is a reaction intermediate in photo-thermo coupled reaction condition too. Comparing with the results under dark, the green light irradiation can lower the temperature of br-H¹³COO* conversion to CO, which indicates this elementary step is activated by light-induced plasmonic effects. The possibility that the effluent ¹³CO is derived from the reaction between re-adsorbed ¹³CO₂* (due to HCOO* dehydrogenation) with H₂ can be ruled out with control experiments (detailed discussions in SI-Section 3.4.1). The same formate TPSR experiments were conducted over the other two samples: Au/Al₂O₃-600 and Au/Al₂O₃-800. The corresponding DRIFTS contour and MS spectra are shown in Fig. S13. The same phenomena were observed for Au/Al₂O₃-600 and Au/Al₂O₃-800: the CO production strongly correlates with br-HCOO* consumption. Additionally, the green light irradiation can effectively lower the temperature of

br-HCOO* conversion to CO, which further proves that the LSPR can activate the br-HCOO* dehydration.

3.3.2. *m*-HCOO* reaction pathway proven by TP-DRIFTS-MS

To unravel temperature-dependent prevailing surface intermediates, the TP-DRIFTS-MS experiments were conducted in both dark and green light irradiation condition. As shown in Fig. 4(a), the prevailing surface species are ¹³CO₃* , H¹³CO₃* and H₂O* at temperature below 170 °C. Fig. 4(b, d) demonstrates the evolutions of br-HCOO* and m-HCOO* IR peak intensities by plotting their first derivative of absorbance with respect to temperature ($\partial\text{Abs.}/\partial\text{Temp.}$) as a function of temperature, respectively. The br-H¹³COO* emerges at ~140 °C and reaches its peak intensity at ~305 °C. By contrast, the m-H¹³COO* shows an abrupt increase at ~225 °C. The derivative of MS-¹³CO with respect as temperature is plotted as a function of temperature to describe the evolution of ¹³CO production. Note that the production of ¹³CO starts from ~225 °C in dark, which is almost the same to the appearance of m-H¹³COO* on the surface and much higher than the emerging of br-H¹³COO*. It strongly indicates the close connection between m-H¹³COO* and ¹³CO product. Similar results are achieved for TP-DRIFTS-MS experiments conducted under green light irradiation. As shown in Fig. 4(e-h), the ¹³CO starts to effluent at temperature of ~185 °C, which is identical to the temperature of m-H¹³COO* formation (~185 °C) but significantly higher than the br-H¹³COO* (~96 °C). Although all the formation temperatures of br-H¹³COO, m-H¹³COO* and CO decrease due to light irradiation, the formation temperature of m-H¹³COO* and ¹³CO remains matched. The disagreement between br-H¹³COO* and ¹³CO formation temperature suggests the br-H¹³COO* can easily formed on the surface but suffers from a high energy barrier to further reduce to CO. Note that during the br-HCOO* TPSR-DRIFTS experiments (Fig. 3), no m-HCOO* can be observed. Therefore, it is more plausible of the direct formation of m-HCOO* from CO₂* and H* rather than the transformation from br-HCOO*, which is different from previous report [11].

The same TP-DRIFTS-MS experiments were also conducted over the other two samples with larger Au NPs. From Fig. S14 (Au/Al₂O₃-600), it can be concluded that the consistency of CO generation temperature and m-HCOO* formation temperature is still valid. The green light irradiation can also significantly reduce the temperature of the formate and CO formation. The same formation temperature strongly suggests the m-HCOO* pathway is still an important reaction pathway in dark and under green light irradiation over Au/Al₂O₃-600. In the case of Au/Al₂O₃-800 (Fig. S15), the situation is slightly different. In Fig. S15(a), the H¹³COO* peak is quite symmetric, which suggests that there is no observable m-H¹³COO* peak during the TP-DRIFTS-MS experiment. It is also demonstrated by Fig. S15(c). By contrast, under green light irradiation, the m-H¹³COO* can be found in the ramping procedure (Fig. S15(e)). Again, the formation temperature of m-H¹³COO* and CO is consistent. The different behaviors of Au/Al₂O₃-800 in dark and under green light irradiation indicates the plasmonic electrons will significantly enhance the formation of m-HCOO* and facilitate the m-formate reaction pathway.

3.3.3. SSITKA-DRIFTS investigation on kinetics of HCOO*

SSITKA-DRIFTS experiments can provide kinetic information of the key reaction intermediates HCOO* group at a steady state. A typical temperature of 300 °C was chosen as the investigation temperature and ¹²CO₂/¹³CO₂ with the identical flow rate were swiftly switched with a 4-way valve; the moment of isotope switch was denoted as t = 0 min in the DRIFTS contours (Fig. 5). As shown in Fig. 5(a, c), br-HCOO* and m-HCOO* can be observed on the surface of the Au/Al₂O₃-400, which agrees with the other DRIFTS contours shown in former sections. In dark (Fig. 5(a, b)), the m-HCOO* decays significantly faster than br-HCOO*. The corresponding exponential decay fittings interpret the kinetic surface lifetimes of 10.76 and 8.13 min for br-HCOO* ad m-HCOO*, respectively. Under green light irradiation (Fig. 5(c, d)), the kinetics of

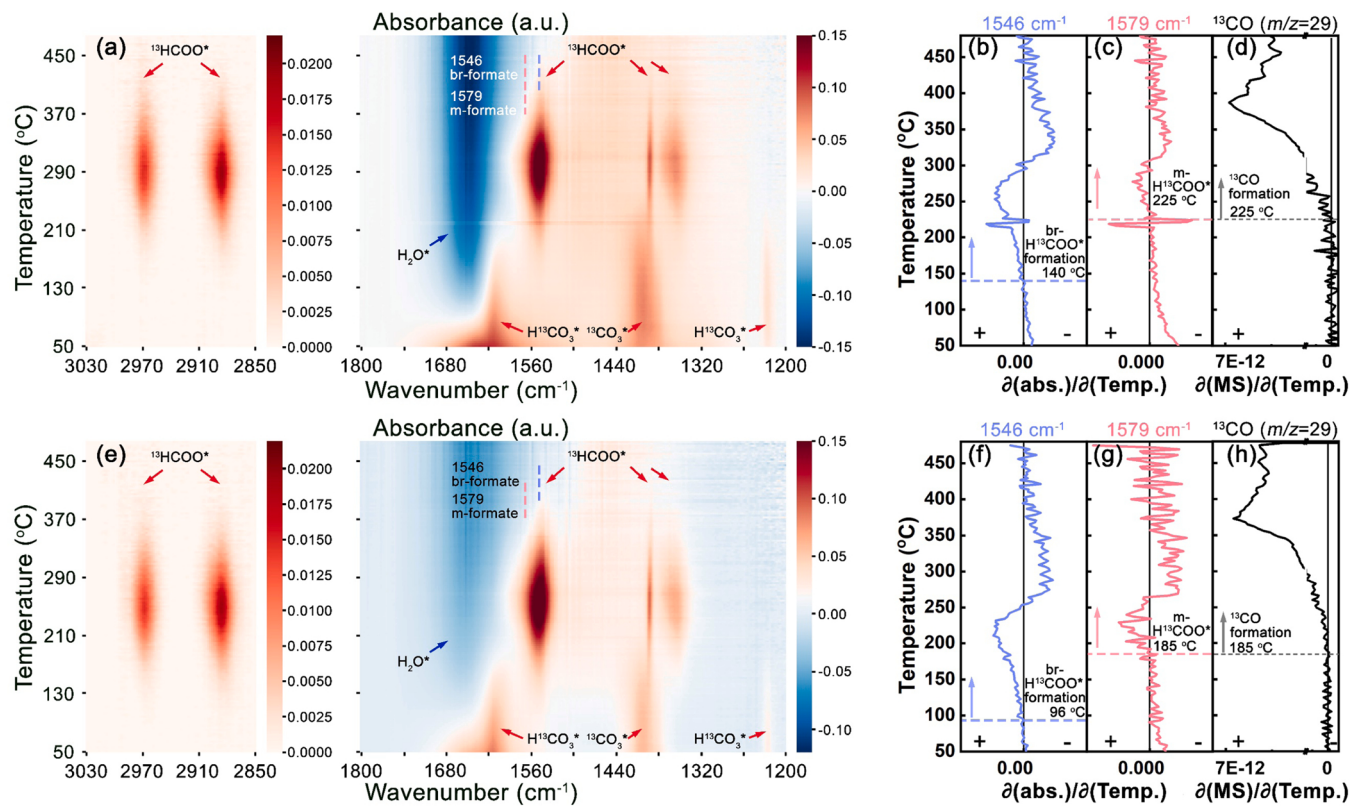


Fig. 4. TP-DRIFTS-MS investigations on $^{13}\text{CO}_2$ hydrogenation from 50° to 480°C over Au/Al₂O₃-400. (a) The DRIFTS contour, corresponding IR peak intensity evolution of (b) br- $\text{H}^{13}\text{COO}^*$ (1546 cm^{-1}), (c) m- H^{13}COO (1579 cm^{-1}) and (d) first derivative of ^{13}CO -MS signal with respect to temperature as a function of temperature in dark. (e) The DRIFTS contour, corresponding IR peak intensity evolution of (f) br- $\text{H}^{13}\text{COO}^*$ (1546 cm^{-1}), (g) m- $\text{H}^{13}\text{COO}^*$ (1579 cm^{-1}) and (h) first derivative of ^{13}CO -MS signal with respect to temperature as a function of temperature under green light irradiation. The MS signal of ^{13}CO has been calibrated against $^{13}\text{CO}_2$.

both br- HCOO^* and m- HCOO^* are significantly accelerated with the corresponding surface lifetimes of 3.95 and 3.22 min. The same SSITKA-DRIFTS experiments were conducted over Au/Al₂O₃-600 and Au/Al₂O₃-800 too (Figs. S16&17). The calculated kinetic surface lifetimes are summarized in Table 1.

To further unravel the correlation between LSPR strength and surface HCOO^* kinetics, it is important to compare the light induced HCOO^* kinetics facilitation across all three samples. Because the larger Au NPs can result in a stronger LSPR effect. During the SSITKA-DRIFTS characterization, it is believed the reaction stays at the constant rate and surface species with constant coverage. Therefore, the SSITKA experiment can measure the reaction activity of single species independent from its abundance on the surface [11,18]. The measured HCOO^* surface lifetime is a reciprocal of the pseudo-first-order reaction rate constant k :

$$k = \tau^{-1} \quad (2)$$

Considering the plasmonic resonance doesn't change the active sites for each reaction intermediates, the plasmonic enhancement (P) on overall, m- HCOO^* and br- HCOO^* reaction rates can be represented by following equations:

$$P_{\text{overall}} = \frac{r_{\text{CO_green}}}{r_{\text{CO_dark}}} \quad (3)$$

$$P_{\text{m-HCOO}^*} = \frac{k_{\text{m-HCOO}^*\text{-dark}}}{k_{\text{m-HCOO}^*\text{-green}}} = \frac{\tau_{\text{m-HCOO}^*\text{-green}}}{\tau_{\text{m-HCOO}^*\text{-dark}}} \quad (4)$$

$$P_{\text{br-HCOO}^*} = \frac{k_{\text{br-HCOO}^*\text{-dark}}}{k_{\text{br-HCOO}^*\text{-green}}} = \frac{\tau_{\text{br-HCOO}^*\text{-green}}}{\tau_{\text{br-HCOO}^*\text{-dark}}} \quad (5)$$

As shown in Fig. 6, the $P_{\text{m-HCOO}^*}$ and $P_{\text{br-HCOO}^*}$ are significantly larger

than P_{overall} . Considering the reaction mechanism is a combination of HCOO^* and COOH^* pathway, this result clearly indicates the LSPR promotes HCOO^* pathway more significantly than COOH^* pathway in the reaction. Moreover, HCOO^* kinetics enhancement also follows the same sequence of LSPR effects strength. It is also worth noticing that the $P_{\text{br-HCOO}^*}$ is larger than $P_{\text{m-HCOO}^*}$ over Au/Al₂O₃-400 and Au/Al₂O₃-600 with relatively smaller Au NPs sizes. While in the case of Au/Al₂O₃-800 with significantly larger Au NPs, the $P_{\text{br-HCOO}^*}$ and $P_{\text{m-HCOO}^*}$ becomes similar. It can be plausibly explained by the combination of two enhancement mechanisms. For smaller Au NPs, the plasmonic resonance decay will excite hot electrons in higher energy, which act as the main enhancement mechanism. Due to the lower energy of antibonding states of br- HCOO^* than m- HCOO^* (Fig. 6(c, d)), the "hot" electrons are more likely inject into br- HCOO^* rather than m- HCOO^* . Therefore, the br- HCOO^* kinetics is more enhanced by LSPR. For larger Au NPs, the LSPR induced strong electromagnetic field becomes the dominated enhancement mechanism, which is less electronic structure sensitive [33,34].

3.4. H/D Kinetic isotope effects (KIE) and equilibrium isotope effects (EIE)

H/D KIE is used to unravel the mechanisms of reaction and the plasmonic enhancement. As shown in Fig. 7, the apparent KIEs are observed smaller than 1 both in dark or under green light irradiation at the temperature of 300 °C. Two results are important to note: (1) Au/Al₂O₃-400 shows a less significant inverse KIE of 0.82/0.84 for dark/light-promoted conditions. Comparatively, for larger Au NP size (Au/Al₂O₃-800), the apparent inverse KIE values and the difference between dark and light-irradiation conditions both become much more evident (0.47/0.60 for dark/light-irradiation condition); (2) the green

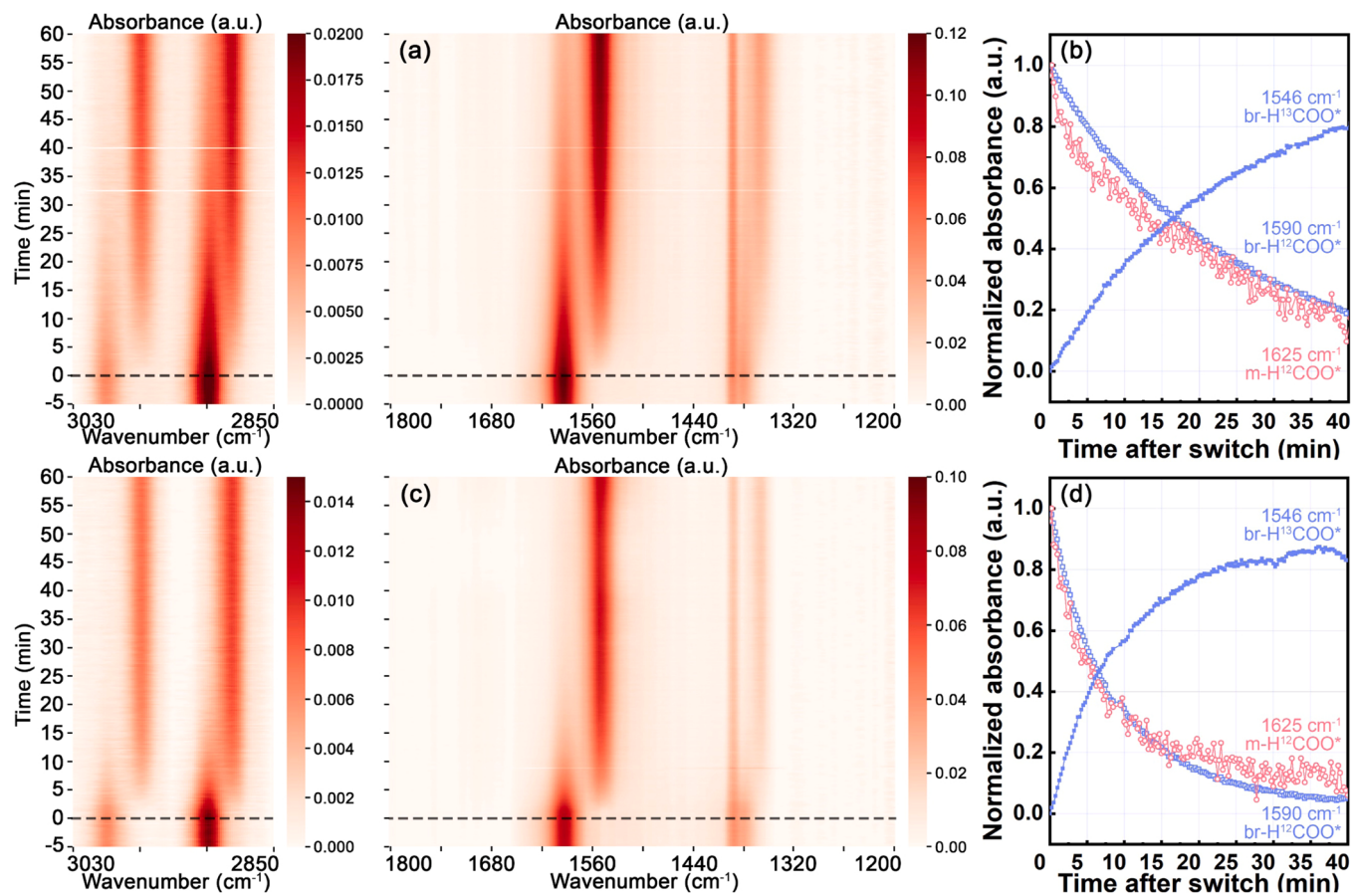


Table 1
Summaries of kinetic parameters derived from SSITKA-DRIFTS experiments at 300 °C.

Sample	Condition	GC	FTIR
		CO yield (mmol g _{cat} ⁻¹ h ⁻¹)	$\tau_{\text{br}-\text{HCOO}^*}$ (min)
Au/Al ₂ O ₃ -400	dark	0.47	11.04
	green	0.57	5.06
Au/Al ₂ O ₃ -600	dark	0.40	12.25
	green	0.60	5.17
Au/Al ₂ O ₃ -800	dark	0.17	26.65
	green	0.36	8.70

light irradiation results in larger apparent KIE values (closer to 1) compared to the counterparts in dark; the increases of apparent KIE values become greater on larger Au NPs. Considering the EIE values are very close to 1 and exhibit small enough difference in dark or under green light irradiation (Fig. S18, Table S3), the qualitative mechanism discussions based on apparent KIE values are good approximation [18].

The reaction pathway and RDS can be interpreted based on the aforementioned results. The noticeable inverse KIE over Au/Al₂O₃-800 suggests the main reaction pathway is likely to be the COOH^{*} pathway with COOH^{*} formation as the RDS, which has also been reported in other investigations [35–38]. Comparatively, the insignificant KIE over Au/Al₂O₃-400 suggests the reaction mechanism is likely to be a combination of COOH^{*} pathway and HCOO^{*} pathway. The HCOO^{*} pathway was reported to show a normal KIE with its RDS of the dehydration step [39,40]. For reaction in dark, the inverse KIE becomes more significant (away from 1) from Au/Al₂O₃-400 to Au/Al₂O₃-800 indicating

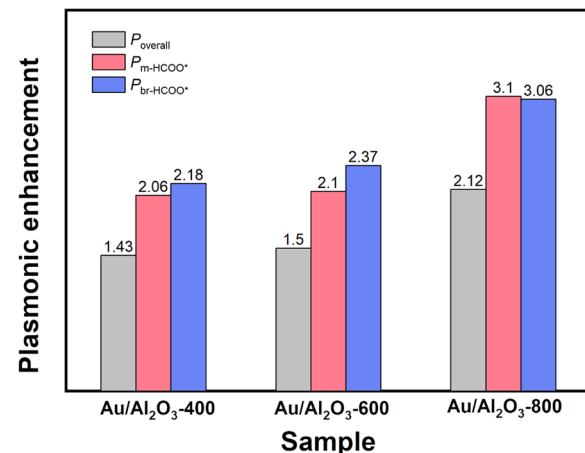


Fig. 6. Plasmonic enhancement ratios on overall reaction rate, m-HCOO* and br-HCOO* kinetics.

the contribution of HCOO^{*} pathway drops when Au NPs becomes larger. In the case of reaction under green light irradiation, the KIE shifts from significant inverse to insignificant, which suggests the proportion of HCOO^{*} pathway in overall reaction become dominant due to plasmonic enhancements. The difference between KIE value with and without light-irradiation also becomes more significant from Au/Al₂O₃-400 to Au/Al₂O₃-800, which agrees with the sequence of stronger LSPR effects on larger Au NPs and strongly support the non-thermal effects of plasmonic enhancements [18,41,42]. The different contributions of formate

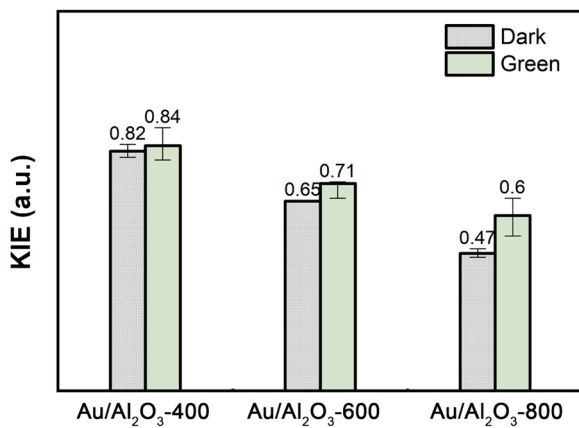


Fig. 7. Apparent H/D kinetic isotope effects (KIE) of RWGS over Au/ γ -Al₂O₃ at different temperatures in dark or under green light irradiation.

and carboxyl pathways to the overall reaction derived from KIE analyses are in consistent with the DRIFTS-SSKTA analyses results in former section. The RDSs of formate and carboxyl pathways also agrees with our DFT calculation results, which will be further discussed in Section 3.5.

3.5. Theoretical calculation

The reaction pathway and plasmonic enhancement mechanism are further supported by the DFT calculation. Au/ γ -Al₂O₃ catalysts are

represented by loading Au₁₃ clusters onto a γ -Al₂O₃ (110) surface. The details of building this slab model are described in the SI-Section 5, and the corresponding optimized structure is shown in Fig. S20. In consistence with experimental results, there are two different kinds of CO₂* adsorbing at Au/ γ -Al₂O₃ interface in monodentate and bridged configurations (m-CO₂* and br-CO₃*). The m-CO₂* and br-CO₃* function as the precursors to further form the m-HCOO* and br-HCOO* after adding an additional H*, respectively. The most energy-favorable m-CO₂* and br-CO₂* geometries are shown in Fig. S18, and the calculated CO₂ adsorption energies (E_{ad}) are -0.74 and -1.25 eV for m-CO₂* and br-CO₂*, respectively. The m-CO₂* adsorbs at the tricoordinate Al site (Al₃C), and by contrast, the br-CO₂* adsorbs at the interface with its two O atoms bonding with Al₃C and Al₄C (four-coordinated Al), respectively. The larger E_{ad} for br-CO₂* than m-CO₂* indicates the higher abundance of br-CO₂* than its counterpart m-CO₂*, which is consistent with DRIFTS results.

Since the direct dissociation CO₂ mechanism is ruled out by experiments (Fig. S9), the DFT calculation here focuses on the carboxyl and formate pathway. Consistent with *in-situ* DRIFTS experimental results, the reaction pathways are classified into m-formate/carboxyl and br-formate/carboxyl pathways starting from m-CO₂* and br-CO₂*, respectively. The calculated reaction profiles are plotted in Fig. 8(a, b) and the energetics are summarized in Table 2 & Table 3. Whether reaction goes along formate or carboxyl pathways are determined by the first hydrogenation step of CO₂*. For m-CO₂*, the formation of monodentate trans-COOH* requires a high activation energy (E_a) of 1.38 eV; by contrast the m-HCOO* only requires a smaller E_a of 0.65 eV after H* diffusion to the adjacent site of C with an E_a of 0.74 eV. Similarly, the br-trans-COOH* formed from br-CO₂* requires an even higher E_a of 1.74 eV

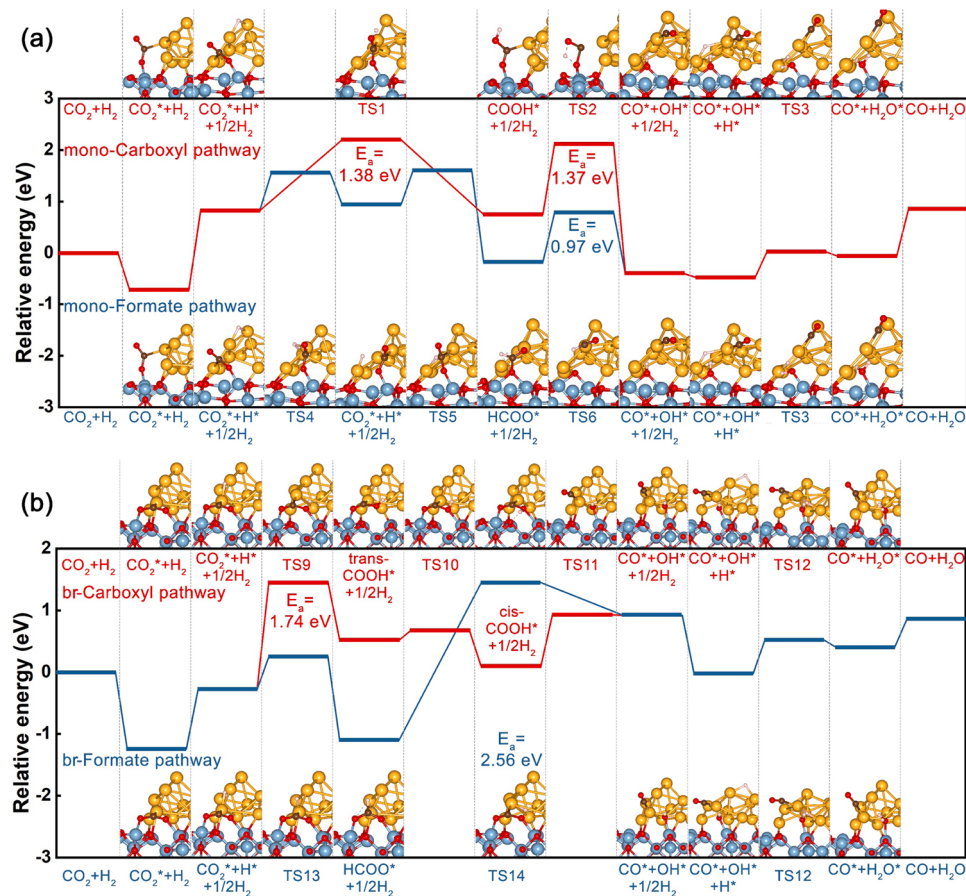


Fig. 8. Calculated reaction profiles of (a) m-formate, m-carboxyl and (b) br-formate, br-carboxyl reaction pathways over Au₁₃/ γ -Al₂O₃(110). The calculated configurations of each elementary steps are presented at the top and bottom of the images. The activation energy (E_a) of RDS in their corresponding reaction pathway is also depicted in the plots. The blue, red, amber, brown and pink spheres represent Al, O, Au, C and H atoms, respectively.

Table 2

Energetics for reaction steps along m-formate and br-formate reaction pathways.

Reaction steps	m-formate pathway		br-formate pathway	
	Reaction energy (eV)	E _a (eV)	Reaction energy (eV)	E _a (eV)
CO ₂ + H ₂ → CO ₂ * + H ₂	-0.74		-1.25	
CO ₂ * + H* + 1/2 H ₂ →	+0.13	+0.74		
CO ₂ * + H* + 1/2H ₂ (H* diffusion on Au)				
CO ₂ * + H* + 1/2H ₂ →	-1.12	+0.65	-0.83	+0.53
HCOO* + 1/2H ₂				
HCOO* + 1/2H ₂ → CO* +	-0.23	+0.97	+2.03	+2.56
OH* + 1/2H ₂				
CO* + OH* + H* → CO* +	+0.42	+0.49	+0.43	+0.55
H ₂ O*				
CO* + H ₂ O* → CO + H ₂ O	+0.91		+0.44	

Table 3

Energetics for reaction steps along m-carboxyl and br-carboxyl reaction pathways.

Reaction steps	m-carboxyl pathway		br-carboxyl pathway	
	Reaction energy (eV)	E _a (eV)	Reaction energy (eV)	E _a (eV)
CO ₂ + H ₂ → CO ₂ * + H ₂	-0.74		-1.25	
CO ₂ * + H* + 1/2H ₂ →	-0.07	+1.38	+0.79	+1.74
trans-COOH* + 1/2H ₂				
trans-COOH* + 1/2H ₂ →			-0.43	+0.16
cis-COOH* + 1/2H ₂				
COOH* + 1/2H ₂ → CO* +	-1.15	+1.37	+0.83	+0.85
OH* + 1/2H ₂				
CO* + OH* + H* → CO* +	+0.42	+0.49	+0.43	+0.55
+ H ₂ O*				
CO* + H ₂ O* → CO + H ₂ O	+0.91		+0.44	

and further transforms into br-cis-COOH* with a small E_a of 0.16 eV; by contrast, the formation of br-HCOO* only requires an E_a of 0.53 eV. Additionally, both m- and br-HCOO* are more stable than their COOH* counterparts by 0.93 and 1.19 eV, respectively. Therefore, it is more energy-favorable to form HCOO* rather than COOH* over Au₁₃/γ-Al₂O₃ from both thermodynamic and kinetic perspectives.

Considering the full reaction profile, for COOH* pathways, the overall RDS is likely to be the elementary step of the COOH* formation. Different from COOH*, the RDS for HCOO* pathway is the HCOO* decomposition to CO* and OH* for both monodentate and bridged configurations showing the E_a of 0.97 and 2.56 eV, respectively. The following H₂O* formation step for both monodentate and bridged configurations only show a small E_a of 0.50 and 0.55 eV. The small E_a of formation and remarkably large E_a of decomposition make the br-HCOO* accumulate on the surface. Also, the smallest overall E_a of the m-HCOO* pathway makes it the most plausible candidate from the perspective of kinetics. It also explains the much higher IR peak observed for br-HCOO* than m-HCOO* in DRIFTS experiments (Fig. 4 and Figs. S14&S15).

Electronic structure analyses can provide insights on the possible plasmonic “hot” electrons-induced enhancement. The PDOS plots of important surface species including CO₂*, HCOO* and COOH* in their monodentate and bridged configurations are presented in Fig. S21(a, b) and Fig. S22(a-d). The grey dash lines represent the energy of 2.4 eV, which is the highest possible energy the plasmonic hot electron can achieve under 532 nm light irradiation. m-HCOO* shows nearly no unoccupied states above fermi energy level (E_f). However, there is a major C2p-O2p orbitals below the upper energy limit of 2.4 eV for br-HCOO*. The difference in the electronic structure suggests the hot electrons are much more likely to inject into and activate the br-HCOO* than m-HCOO*. Since the further conversion of br-HCOO* is the plausible RDS for this reaction pathway, the plasmonic “hot”

electron injection is likely to significantly enhance the overall reaction kinetics. There is no fundamental difference in electronic structures between m-CO₂*, br-CO₂*. Both two types of CO₂* are expected to be activated, while the negatively charged CO₂* participates in subsequent conversion more readily [43,44], which explains the lower formation temperature for br- and m-HCOO*. Similarly, both br-COOH* and m-COOH* are likely to be activated by “hot” electron injection from the perspective of electronic structure. However, the RDS for carboxyl pathway is proven to be its formation rather its decomposition and the unoccupied orbitals of CO₂* below 2.4 eV shows very small density in term of states (Fig. S21((a, b)), which results in a weak excitation. Therefore, the plasmon-enhancement on COOH* pathway is less prominent. To further deduce how “hot” electron injection activates the br-HCOO*, the COHP analyses of O-Al bonds of br-HCOO* and m-HCOO* are plotted in the Fig. S21(c, d) with the configurations shown in Fig. S21((e, f), respectively. Since the bond population is presented in -COHP, the bonding and antibonding states are shown in the right and left side of the plot, respectively. Note that the C-O antibonding states of m-HCOO* locate above 2.4 eV, the kinetics of m-HCOO* decomposition is expected to not be affected by “hot” electrons. On the contrary, in the case the br-HCOO*, the C-O shows much higher antibonding state populations underneath the 2.4 eV limit. The electronic structure of br-HCOO* suggests the plasmonic “hot” electron can much more efficiently activate the dehydration of br-HCOO* to CO* than m-HCOO*.

In summary, DFT calculation results suggest the RWGS reaction mainly follows the HCOO* pathway way over Au/γ-Al₂O₃ under both dark and light irradiation conditions. The RDS for formate pathway is its decomposition to CO* and OH*. The m-HCOO* shows the smallest overall E_a, while its abundance is limited by thermodynamics (its weak absorption). Under green light irradiation, the plasmon-excited electrons are more likely to inject into unoccupied antibonding orbitals of br-HCOO* than m-HCOO* and facilitate its further hydrogenation. These calculation results greatly agree with the *in-situ* DRIFTS and SSITKA experimental results in dark and under green light irradiation.

4. Conclusion

CO₂ hydrogenation reactions were investigated over Au/Al₂O₃ with different Au NPs sizes under pure thermal and photo-thermo coupled reaction conditions. The smaller Au NPs shows higher reaction activity than larger Au NPs in dark. While under external green light irradiation, the plasmonic enhancement is more significant over larger Au NPs. A maximum of 211.8 % reaction rate enhancement is achieved by external light induced plasmonic effects. The reaction mechanisms are proven to be a combination of formate and carboxyl pathways via *in-situ* DRIFTS/ SSITKA and KIE analyses. Moreover, the proportion of m-HCOO* pathway contributions is higher on smaller Au NPs. The br-HCOO* is proven to be a reaction intermediate and contribute to the overall reaction rate. Green light irradiation shows the preferential promotion effects on formate intermediate kinetics. The main plasmon-thermo coupling mechanisms that are likely to be “hot” electrons injection mainly for smaller Au NPs and resonance energy transfer enhancements for larger Au NPs.

CRediT authorship contribution statement

Ke Wang: Conceptualization, Funding acquisition, Investigation, Formal analysis, Methodology, Writing – original draft. **Shibo Shao:** Investigation, Formal analysis, Methodology, Writing – review & editing. **Yanrong Liu:** Investigation, Formal analysis. **Mengyu Cao:** Investigation, Formal analysis, Methodology. **Jialin Yu:** Investigation, Formal analysis. **Cher Hon Lau:** Supervision, Writing – review & editing. **Ying Zheng:** Conceptualization, Supervision, Writing – review & editing. **Xianfeng Fan:** Conceptualization, Funding acquisition, Project administration, Supervision, Writing – review & editing.

Declaration of Competing Interest

The authors declare that they have no known competing financial interests or personal relationships that could have appeared to influence the work reported in this paper.

Data availability

Data will be made available on request.

Acknowledgements

The authors thank the financial supports from the Innovation Academy for Green Manufacture, Chinese Academy of Sciences (IAGM2022D12), the National Natural Science Foundation of China (22208348, 22278402), the UK research council EPSRC (EP/V041665/1) and the school of engineering, the University of Edinburgh. Dr. Laetitia Pichevin from the school of geoscience, the University of Edinburgh is much appreciated for the assistance of ICP-OES tests. Dr. David Miller from the school of chemistry, the University of St. Andrews is appreciated for the help on HAADF-STEM characterizations. The authors thank the technical helps from Mr. Fergus Dingwall on lab works. This work has made use of the resources provided by the Edinburgh Compute and Data Facility (ECDF) (<http://www.ecdf.ed.ac.uk/>) and Compute Canada (www.computecanada.ca). Sincerely appreciate Prof. Suojiang Zhang (IPE, CAS) for his careful academic guidance and great support.

Appendix A. Supporting information

Supplementary data associated with this article can be found in the online version at [doi:10.1016/j.apcatb.2023.122531](https://doi.org/10.1016/j.apcatb.2023.122531).

References

- [1] A. Dominguez-Ramos, A. Irabien, The role of power-to-gas in the European Union, *Green Chem. Eng.* 1 (2020) 6–8, <https://doi.org/10.1016/j.gce.2020.10.002>.
- [2] M. Sun, B. Zhao, R. Yang, F. Chen, Y. Yu, B. Zhang, Photoinduced H2 heterolytic to form Mo₂NH_x active species for CO₂ reduction, *ACS Energy Lett.* 6 (2021) 2024–2029, <https://doi.org/10.1021/acsenergylett.1c00645>.
- [3] S. Wang, A.A. Tountas, W. Pan, J. Zhao, L. He, W. Sun, D. Yang, G.A. Ozin, CO₂ footprint of thermal versus photothermal CO₂ catalysis, *Small* 17 (2021), e2007025, <https://doi.org/10.1002/smll.202007025>.
- [4] Z. Wu, C. Li, Z. Li, K. Feng, M. Cai, D. Zhang, S. Wang, M. Chu, C. Zhang, J. Shen, Z. Huang, Y. Xiao, G.A. Ozin, X. Zhang, L. He, Niobium and titanium carbides (MXenes) as superior photothermal supports for CO₂ photocatalysis, *ACS Nano* 15 (2021) 5696–5705, <https://doi.org/10.1021/acsnano.1c00990>.
- [5] J.Q. Zhang, Y.G. Li, J.M. Sun, H.J. Chen, Y.Z. Zhu, X.L. Zhao, L.C. Zhang, S. J. Wang, H.Y. Zhang, X.G. Duan, L. Shi, S. Zhang, P. Zhang, G.S. Shao, M.B. Wu, S. B. Wang, H.Q. Sun, Regulation of energetic hot carriers on Pt/TiO₂ with thermal energy for photothermal catalysis, *Appl. Catal. B* 309 (2022), 121263, <https://doi.org/10.1016/j.apcatb.2022.121263>.
- [6] H. Ge, Y. Kuwahara, K. Kusu, Z.F. Bian, H. Yamashita, Ru/H_xMoO_{3-y} with plasmonic effect for boosting photothermal catalytic CO₂ methanation, *Appl. Catal. B* 317 (2022), 121734, <https://doi.org/10.1016/j.apcatb.2022.121734>.
- [7] J. Zhu, W. Shao, X. Li, X. Jiao, J. Zhu, Y. Sun, Y. Xie, Asymmetric triple-atom sites confined in ternary oxide enabling selective CO₂ photothermal reduction to acetate, *J. Am. Chem. Soc.* 143 (2021) 18233–18241, <https://doi.org/10.1021/jacs.1c08033>.
- [8] Z. Zhang, C. Mao, D.M. Meira, P.N. Duchesne, A.A. Tountas, Z. Li, C. Qiu, S. Tang, R. Song, X. Ding, J. Sun, J. Yu, J.Y. Howe, W. Tu, L. Wang, G.A. Ozin, New black indium oxide-tandem photothermal CO₂-H₂ methanol selective catalyst, *Nat. Commun.* 13 (2022) 1512, <https://doi.org/10.1038/s41467-022-29222-7>.
- [9] S. Fang, Y.H. Hu, Thermo-photo catalysis: a whole greater than the sum of its parts, *Chem. Soc. Rev.* 51 (2022) 3609–3647, <https://doi.org/10.1039/d1cs00782c>.
- [10] F. Zhang, Y.-H. Li, M.-Y. Qi, Y.M.A. Yamada, M. Anpo, Z.-R. Tang, Y.-J. Xu, Photothermal catalytic CO₂ reduction over nanomaterials, *Chem. Catal.* 1 (2021) 272–297, <https://doi.org/10.1016/j.chemcat.2021.01.003>.
- [11] N.C. Nelson, M.T. Nguyen, V.A. Glezakou, R. Rousseau, J. Szanyi, Carboxyl intermediate formation via an in situ-generated metastable active site during water-gas shift catalysis, *Nat. Catal.* 2 (2019) 916–924, <https://doi.org/10.1038/s41929-019-0343-2>.
- [12] N.C. Nelson, J. Szanyi, Heterolytic hydrogen activation: understanding support effects in water-gas shift, hydrodeoxygenation, and CO oxidation catalysis, *ACS Catal.* 10 (2020) 5663–5671, [https://doi.org/10.1021/acs catal.0c01059](https://doi.org/10.1021/acs катал.0c01059).
- [13] L.F. Bobadilla, J.L. Santos, S. Ivanova, J.A. Odriozola, A. Urakawa, Unravelling the role of oxygen vacancies in the mechanism of the reverse water-gas shift reaction by Operando DRIFTS and ultraviolet-visible spectroscopy, *ACS Catal.* 8 (2018) 7455–7467, <https://doi.org/10.1021/acs catal.8b02121>.
- [14] X. Wang, H. Shi, J.H. Kwak, J. Szanyi, Mechanism of CO₂ hydrogenation on Pd/Al₂O₃ catalysts: kinetics and transient DRIFTS-MS studies, *ACS Catal.* 5 (2015) 6337–6349, <https://doi.org/10.1021/acs catal.5b01464>.
- [15] Z.Y. Zhang, T. Zhang, R.K. Wang, B. Yu, Z.Y. Tang, H.Y. Zheng, D. He, T. Xie, Z. Hu, Photo-enhanced dry reforming of methane over Pt-Au/P25 composite catalyst by coupling plasmonic effect, *J. Catal.* 413 (2022) 829–842, <https://doi.org/10.1016/j.jcat.2022.07.028>.
- [16] K. Feng, Y.N. Wang, M. Guo, J.P. Zhang, Z.W. Li, T.Y. Deng, Z.H. Zhang, B.H. Yan, In-situ/operando techniques to identify active sites for thermochemical conversion of CO₂ over heterogeneous catalysts, *J. Energy Chem.* 62 (2021) 153–171, <https://doi.org/10.1016/j.jechem.2021.03.054>.
- [17] Y. Li, R.Z. Li, Z.H. Li, Y.Q. Xu, H. Yuan, S.X. Ouyang, T.R. Zhang, Recent advances in photothermal CO_x conversion, *Sol. RRL* 6 (2022) 2200493, <https://doi.org/10.1002/solr.202200493>.
- [18] K. Wang, M.Y. Cao, J.B. Lu, Y. Lu, C.H. Lau, Y. Zheng, X.F. Fan, Operando DRIFTS-MS investigation on plasmon-thermal coupling mechanism of CO₂ hydrogenation on Au/TiO₂: the enhanced generation of oxygen vacancies, *Appl. Catal. B* 296 (2021), 120341, <https://doi.org/10.1016/j.apcatb.2021.120341>.
- [19] B.W. Deng, H. Song, K. Peng, Q. Li, J.H. Ye, Metal-organic framework-derived Ga-Cu/CeO₂ catalyst for highly efficient photothermal catalytic CO₂ reduction, *Appl. Catal. B* 298 (2021), 120519, <https://doi.org/10.1016/j.apcatb.2021.120519>.
- [20] K. Wang, J.B. Lu, Y. Lu, C.H. Lau, Y. Zheng, X.F. Fan, Unravelling the C-C coupling in CO₂ photocatalytic reduction with H₂O on Au/TiO_{2-x} combination of plasmonic excitation and oxygen vacancy, *Appl. Catal. B* 292 (2021), 120147, <https://doi.org/10.1016/j.apcatb.2021.120147>.
- [21] X.B. Li, W.W. Wang, F. Dong, Z.Q. Zhang, L. Han, X.D. Luo, J.T. Huang, Z.J. Feng, Z. Chen, G.H. Jia, T.R. Zhang, Recent advances in noncontact external-field-assisted photocatalysis: from fundamentals to applications, *ACS Catal.* 11 (2021) 4739–4769, <https://doi.org/10.1021/acs catal.0c05354>.
- [22] C.Y. Xu, X.H. Zhang, M.N. Zhu, L. Zhang, P.F. Sui, R.F. Feng, Y.W. Zhang, J.L. Luo, Accelerating photoelectric CO₂ conversion with a photothermal wavelength-dependent plasmonic local field, *Appl. Catal. B* 298 (2021), <https://doi.org/10.1016/j.apcatb.2021.120533>.
- [23] P. Giannozzi, O. Andreussi, T. Brumme, O. Bunau, M. Buongiorno Nardelli, M. Calandri, R. Car, C. Cavazzoni, D. Ceresoli, M. Cococcioni, N. Colonna, I. Carnimeo, A. Dal Corso, S. de Gironcoli, P. Delugas, R.A. DiStasio Jr., A. Ferretti, A. Floris, G. Fratesi, G. Fugallo, R. Gebauer, U. Gerstmann, F. Giustino, T. Gorni, J. Jia, M. Kawamura, H.Y. Ko, A. Kokalj, E. Kucukbenli, M. Lazzari, M. Marsili, N. Marzari, F. Mauri, N.L. Nguyen, H.V. Nguyen, A. Otero-de-la-Roza, L. Paulatto, S. Ponce, D. Rocca, R. Sabatini, B. Santra, M. Schlipf, A.P. Seitsonen, A. Smogunov, I. Timrov, T. Thonhauser, P. Umari, N. Vast, X. Wu, S. Baroni, Advanced capabilities for materials modelling with Quantum ESPRESSO, *J. Phys. Condens. Matter* 29 (2017), 465901, <https://doi.org/10.1088/1361-648X/aa8f79>.
- [24] J.P. Perdew, K. Burke, M. Ernzerhof, Generalized gradient approximation made simple, *Phys. Rev. Lett.* 77 (1996) 3865–3868, <https://doi.org/10.1103/PhysRevLett.77.3865>.
- [25] S. Grimme, J. Antony, S. Ehrlich, H. Krieg, A consistent and accurate ab initio parametrization of density functional dispersion correction (DFT-D) for the 94 elements H-Pu, *J. Chem. Phys.* 132 (2010), 154104, <https://doi.org/10.1063/1.3382344>.
- [26] A. Dal Corso, Pseudopotentials periodic table: from H to Pu, *Comput. Mater. Sci.* 95 (2014) 337–350, <https://doi.org/10.1016/j.commatsci.2014.07.043>.
- [27] S. Smidstrup, A. Pedersen, K. Stokbro, H. Jonsson, Improved initial guess for minimum energy path calculations, *J. Chem. Phys.* 140 (2014), 214106, <https://doi.org/10.1063/1.4878664>.
- [28] S. Maintz, V.L. Deringer, A.L. Tchougrueff, R. Dronskowski, LOBSTER: a tool to extract chemical bonding from plane-wave based DFT, *J. Comput. Chem.* 37 (2016) 1030–1035, <https://doi.org/10.1002/jcc.24300>.
- [29] K. Momma, F. Izumi, VESTA 3 for three-dimensional visualization of crystal, volumetric and morphology data, *J. Appl. Crystallogr.* 44 (2011) 1272–1276, <https://doi.org/10.1107/s0021889811038970>.
- [30] R. Burch, Gold catalysts for pure hydrogen production in the water-gas shift reaction: activity, structure and reaction mechanism, *Phys. Chem. Chem. Phys.* 8 (2006) 5483–5500, <https://doi.org/10.1039/b607837k>.
- [31] F.C. Meunier, D. Tibiletti, A. Goguet, S. Shekhtman, C. Hardacre, R. Burch, On the complexity of the water-gas shift reaction mechanism over a Pt/CeO₂ catalyst: effect of the temperature on the reactivity of formate surface species studied by operando DRIFT during isotopic transient at chemical steady-state, *Catal. Today* 126 (2007) 143–147, <https://doi.org/10.1016/j.cattod.2006.10.003>.
- [32] H.L. Huynh, W.M. Tucho, Z.X. Yu, Structured NiFe catalysts derived from in-situ grown layered double hydroxides on ceramic monolith for CO₂ methanation, *Green Energy Environ.* 5 (2020) 423–432, <https://doi.org/10.1016/j.gee.2020.09.004>.
- [33] B. Seemala, A.J. Therrien, M. Lou, K. Li, J.P. Finzel, J. Qi, P. Nordlander, P. Christopher, Plasmon-mediated catalytic O₂ dissociation on ag nanostructures: hot electrons or near fields? *ACS Energy Lett.* 4 (2019) 1803–1809, <https://doi.org/10.1021/acsenergylett.9b00990>.
- [34] D. Mateo, J.L. Cerrillo, S. Durini, J. Gascon, Fundamentals and applications of photo-thermal catalysis, *Chem. Soc. Rev.* 50 (2021) 2173–2210, <https://doi.org/10.1039/d0cs00357c>.
- [35] S. Yu, P.K. Jain, Isotope effects in plasmonic photosynthesis, *Angew. Chem. Int. Ed.* 59 (2020) 22480–22483, <https://doi.org/10.1002/anie.202011805>.
- [36] J.A. Loiland, M.J. Wulfers, N.S. Marinkovic, R.F. Lobo, Fe/γ-Al₂O₃ and Fe-K/γ-Al₂O₃ as reverse water-gas shift catalysts, *Catal. Sci. Technol.* 6 (2016) 5267–5279, <https://doi.org/10.1039/c5cy0211a>.

- [37] A. Karelovic, G. Galdames, J.C. Medina, C. Yevenes, Y. Barra, R. Jimenez, Mechanism and structure sensitivity of methanol synthesis from CO₂ over SiO₂-supported Cu nanoparticles, *J. Catal.* 369 (2019) 415–426, <https://doi.org/10.1016/j.jcat.2018.11.012>.
- [38] E.L. Kunkes, F. Stuett, F. Abild-Pedersen, R. Schlogl, M. Behrens, Hydrogenation of CO₂ to methanol and CO on Cu/ZnO/Al₂O₃: is there a common intermediate or not? *J. Catal.* 328 (2015) 43–48, <https://doi.org/10.1016/j.jcat.2014.12.016>.
- [39] S. Kwon, T.C. Lin, E. Iglesia, Elementary steps and site requirements in formic acid dehydration reactions on anatase and rutile TiO₂ surfaces, *J. Catal.* 383 (2020) 60–76, <https://doi.org/10.1016/j.jcat.2019.12.043>.
- [40] S. Kwon, T.C. Lin, E. Iglesia, Formic acid dehydration rates and elementary steps on lewis acid-base site pairs at anatase and rutile TiO₂, *Surf., J. Phys. Chem. C* 124 (2020) 20161–20174, <https://doi.org/10.1021/acs.jpcc.0c05721>.
- [41] Z.J. Wang, H. Song, H. Liu, J. Ye, Coupling of solar energy and thermal energy for carbon dioxide reduction: status and prospects, *Angew. Chem. Int. Ed.* 59 (2020) 8016–8035, <https://doi.org/10.1002/anie.201907443>.
- [42] P. Christopher, H. Xin, A. Marimuthu, S. Linic, Singular characteristics and unique chemical bond activation mechanisms of photocatalytic reactions on plasmonic nanostructures, *Nat. Mater.* 11 (2012) 1044–1050, <https://doi.org/10.1038/nmat3454>.
- [43] W. Taifan, J.F. Boily, J. Baltrusaitis, Surface chemistry of carbon dioxide revisited, *Surf. Sci. Rep.* 71 (2016) 595–671, <https://doi.org/10.1016/j.surfrep.2016.09.001>.
- [44] K. Wang, J.L. Fu, Y. Zheng, Insights into photocatalytic CO₂ reduction on C₃N₄: strategy of simultaneous B, K co-doping and enhancement by N vacancies, *Appl. Catal. B* 254 (2019) 270–282, <https://doi.org/10.1016/j.apcatb.2019.05.002>.